Available online at www.sciencedirect.com
ScienceDirect
Journal of Sound and Vibration 306 (2007) 400–418
JOURNAL OF SOUND AND VIBRATION
www.elsevier.com/locate/jsvi

Free response of a system with negative viscous damping and displacement-dependent dry friction damping ☆

Aldo A. Ferri*, Wayne E. Whiteman[1]

School of Mechanical Engineering, Georgia Institute of Technology, Atlanta, GA 30332-0405, USA

Received 24 February 2005; received in revised form 20 March 2007; accepted 21 March 2007
Available online 19 July 2007

Abstract

A stability analysis is conducted of an autonomous single-degree-of-freedom system damped with negative viscous damping and a displacement-dependent Coulomb friction force. The geometry of the dry friction damping element yields a friction force that grows linearly with the system displacement. The most direct application of this system is in the study of a turbomachinery blade with shroud interfaces designed to achieve this geometry. Recent studies have shown that the damping of systems with this type of displacement-dependent dry friction force resembles linear structural damping and suggests that this arrangement may be an effective means of flutter suppression in these turbine and fan blade applications. For this study, the inclusion of negative viscous damping is used in order to approximate destabilizing aerodynamic forces. An exact analysis is conducted to determine the stability of this autonomous system. Results show that energy losses from the displacement-dependent dry friction damper are large enough to achieve local and even global stability under certain conditions.

1. Introduction

In this paper, an analysis is performed to determine the stability conditions of a beam-like structure with a displacement-dependent dry friction damper attached. The geometry of the dry friction damping element yields a normal force across the friction interface that increases linearly with the transverse beam displacement due to an inclined plane or "ramp" configuration. Such frictional systems, often termed "linear-Coulomb-damped" systems have been studied by a number of authors [1–6]. The primary consideration of this paper is the effectiveness of this type of friction damping to counter aeroelastic instabilities such as flutter. Perhaps the most direct application of this system is in the study of a turbomachinery blade with shroud interfaces properly designed to affect displacement-dependent normal loads on the frictional interfaces.

☆ Expanded version of a paper presented at the ASME Design Engineering and Technical Conferences, Chicago, Illinois, September 2–6, 2003.

*Corresponding author. Tel.: +1 404 894 7403; fax: +1 404 894 8496.
E-mail addresses: al.ferri@me.gatech.edu (A.A. Ferri), wayne.whiteman@me.gatech.edu (W.E. Whiteman).
[1]Tel.: +1 404 894 3218.

0022-460X/$ - see front matter © 2007 Elsevier Ltd. All rights reserved.
doi:10.1016/j.jsv.2007.03.090

The suppression of flutter through use of dry friction damping has received considerable attention in the past. Due to the nonlinear characteristics of dry friction, the standard practice is to keep both the friction model and the aerodynamic model as simple as possible. For example, Sinha and Griffin [7] and Ferri and Dowell [8] used constant-magnitude normal loads and negative viscous damping to model the destabilizing aerodynamic forces present in turbine blades. Both studies showed that it was possible to create domains of stability about the origin, but that sufficiently large disturbances could always lead to unbounded response. The reason for this is that the energy dissipation from a frictional interface with constant normal loads grows linearly with slip displacement amplitudes. Conversely, the energy input from negative viscous damping grows like the square of the slip displacement amplitude. Consequently, there is at best only a limited domain over which the dry friction damper can effectively suppress flutter.

When the friction forces are allowed to increase linearly with the slip displacement, the energy loss from the frictional interface also grows like the square of the slip displacement amplitude. In that respect, the damping supplied from a liner-Coulomb-damping element resembles *linear structural damping*. Linear structural damping is often modeled by a complex-stiffness term. The merits and weaknesses of this so-called *Kimball–Lovell complex-stiffness model* have been discussed by several authors [9–11]. While adequate for the case of harmonic excitation, a nonlinear damping model is required in the case of transient response. The damping law must produce a damping force that is proportional to displacement, but 180° out of phase with the slip velocity. This is exactly the case with linear-Coulomb friction in the case of zero preload. (As discussed in this paper, the presence of preload presents a number of significant differences.) Thus, one of the interesting aspects of this work is a careful examination of the ability of positive "linear structural damping" to overcome "negative viscous damping." In this way, the work is closely related to the use of complex stiffnesses in the determination of flutter boundaries in aeroelasticity; see, for example, descriptions of the "V-g" method in the texts of Dowell et al. [12] and Bisplinghoff and Ashley [13].

Negative viscous damping is often used to model destabilizing aerodynamic forces, which are in-phase with velocity. Although crude, the validity of this simplification has been examined by several authors. For example, Sinha et al. [14] used an accurate aerodynamic model in the study of torsional blade flutter suppression through friction damping. Using constant normal forces and a frequency-domain analysis, their results showed good qualitative agreement with earlier work using negative viscous damping. In Ref. [15], Whiteman and Ferri studied the suppression of coupled bending-torsion flutter using linear-Coulomb damping. Their study used a relatively sophisticated state-variable model of aerodynamics, coupled to a two-degree-of-freedom blade cross-sectional model. Again, the results were qualitatively similar to those found using negative viscous damping. In addition, the study confirmed that linear-Coulomb damping could suppress flutter over a much wider range of initial conditions than a system with constant normal forces. Due to the complexity of the model, however, it was not possible to gain much insight into the nonlinear dynamics underlying the observed behavior. The goal of the present paper is to simplify the model and then examine the dynamics of the system in detail.

In the following section, the simplified nondimensional equations of motion are developed and shown to be piecewise-linear in nature. This piecewise-linear structure is exploited to develop exact solutions for systems with and without preload. As discussed in the review article by Ferri [16], the use of exact solutions in dry friction-damped systems has been used effectively by a number of authors. Natsiavas, for example, has studied a variety of piecwise-linear systems using this approach; see, for example [17,18]. Particularly relevant to the present work is that of Shaw [19], where a system with constant normal loads was studied under the influence of harmonic excitation. Shaw considered both positive and negative viscous damping. Caughey and Vijayaraghavan [10] studied the free and forced response of a linear-Coulomb-damped system without viscous damping. Their study showed that the ratios of successive peak displacements in a free response was equal to a constant, just as in the case of viscous damping. Beucke and Kelly [1] extended this analysis to systems that had linear-Coulomb friction and positive viscous damping. Importantly, they also included a preload friction component that was omitted from the model used by Caughey and Vijayaraghavan. Beucke and Kelly compared various equivalent linear damping approximations against their exact solutions.

In a later study, Inaudi et al. [20] generalized the linear-Coulomb damping model to include all nonlinear systems that are piecewise linear in a finite number of *cones* in the state space. Such systems were shown to be *homogeneous of order one*. This means that if $x(t)$ is a solution to the nonlinear governing equation with initial

condition x_0 and forcing $w(t)$, then $\alpha x(t)$ is the response solution corresponding to the scaled initial condition and forcing, αx_0 and $\alpha w(t)$, respectively. Their study used linear-Coulomb-damped systems as an example, but did not consider preload, which destroys the homogeneity property. It is worth noting that their study also used an example of semi-active viscous damping, but did not include viscous damping in their linear-Coulomb-damped model.

In this paper, the combined influence of frictional preload and viscous damping is explicitly considered. While the emphasis of the study is stability of free response under the influence of *negative viscous damping*, the analytical results hold for negative *and* positive viscous damping. Also, the cases of underdamped, critically damped, and overdamped systems are considered. The effectiveness of linear-Coulomb friction in stabilizing such systems is presented in Section 4 for a wide range of system parameters. Conclusions are presented in Section 5.

2. Model development

Fig. 1 shows the model to be studied. The clamped–free beam is assumed to be uniform in cross-section, having mass per unit length, m, elastic modulus E, and cross-sectional area moment, I. The equations of motion for such a system have been developed in Refs. [4,5]. Here a brief review is presented.

The beam flexural displacement $w(x,t)$ can be approximated as

$$w(x,t) = \sum_{i=1}^{M} z_i(t)\phi_i(x), \tag{1}$$

where x is the spatial coordinate measured from the clamped end of the beam, t is time, M is the number of assumed modes, and $z_i(t)$ is the modal amplitude of the ith assumed mode for the beam in flexure, $\phi_i(x)$.

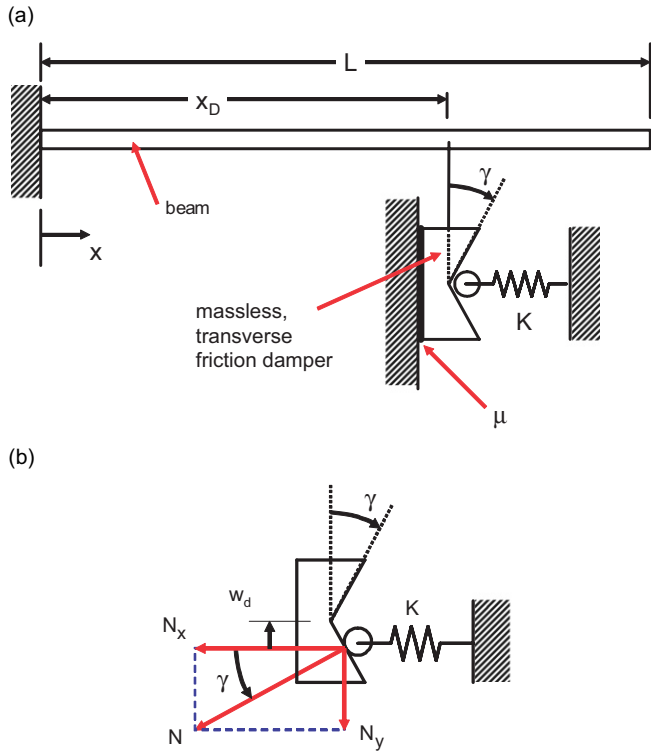

Fig. 1. (a) Flexural beam with transverse friction damper attached and (b) force components.

The assumed modes are taken to be the exact fixed–free eigenmodes of a uniform clamped–free beam:

$$\phi_i(x) = \frac{1}{\sqrt{mL}}\left\{\cosh\frac{\beta_i x}{L} - \cos\frac{\beta_i x}{L} - \left(\frac{\cosh\beta_i + \cos\beta_i}{\sinh\beta_i + \sin\beta_i}\right)\left(\sinh\frac{\beta_i x}{L} - \sin\frac{\beta_i x}{L}\right)\right\}, \tag{2}$$

where β_i is the ith root of the characteristic equation:

$$\cosh\beta\cos\beta + 1 = 0.$$

For definiteness, it is assumed that the units of the modal amplitudes, $z_i(t)$, are length, and that the assumed modes, $\phi_i(x)$, are dimensionless. The scaling factor used in Eq. (2) serves to normalize the assumed modes, thereby leading to unit-valued modal masses.

The friction-damped beam of Fig. 1a can be treated as a uniform linear beam with a point force F_D exerted by the friction damper at the coordinate $x = x_D$. The governing equations for such a system are given by the well-known system of modal equations

$$m_i\left[\ddot{z}_i + 2\zeta_i\omega_i\dot{z}_i + \omega_i^2 z_i\right] = F_D\phi_i(x_D) \quad \text{for } i = 1, M, \tag{3}$$

where m_i, and ω_i are the modal mass and the natural frequency, respectively, for the ith assumed beam mode. The model also provides for the presence of viscous damping in the form of modal damping ratios, ζ_i.

Fig. 1b shows the force components N_x and N_y caused by the spring and roller. The transverse force N_x is the normal force perpendicular to the sliding interface and is given by

$$N_x = N_0 + K|w_d|\tan\gamma, \tag{4}$$

where w_d is the transverse displacement of the beam (and, thus, of the attached friction damper) at the location $x = x_D$:

$$w_d = \sum_{i=1}^{M} z_i(t)\phi_i(x_D). \tag{5}$$

Note that N_x is comprised of two parts: the first part, N_0, is the "preload" present in the spring while the second part grows linearly with the damper displacement due to the ramp angle γ. Referring to Fig. 1b, the tangential component of the roller force, N_y, is given by

$$N_y = (N_x\tan\gamma)\mathrm{sgn}(w_d), \tag{6}$$

where the signum function is given by $\mathrm{sgn}(w_d) = +1$, 0, and -1 for w_d greater than, equal to, or less than zero, respectively.

The total upward force exerted by the friction element on the beam at location $x = x_D$ is given by

$$F_D = -\mu N_x\,\mathrm{sgn}(\dot{w}_d) - N_y. \tag{7}$$

The first part of F_D is the Coulomb friction force having magnitude μN_x, where μ is the sliding coefficient of friction (assumed to be equal to the static coefficient of friction) and N_x is the normal force across the sliding interface. The second part of F_D is the tangential component of the roller force, N_y. As seen in Eq. (6), N_y is small for small ramp angles. However, for larger ramp angles, this force has a significant effect on the equivalent stiffness of the system and on the occurrence of sticking of the frictional interface.

Although Eq. (3) appears to be uncoupled, they are coupled through the friction damping force since, as seen in Eq. (5), the displacement of the beam at location $x = x_D$ depends on all M assumed modes. For the case of a single beam mode model, $M = 1$, the equation of motion is given explicitly by the second-order equation

$$\begin{aligned} m_n\left[\ddot{z}_n(t) + 2\zeta_n\omega_n\dot{z}_n(t) + \omega_n^2 z_n(t)\right] = &-\left\{\left(N_0 + K\tan\gamma\phi_D\left|z_n(t)\right|\right)\phi_D\tan\gamma\,\mathrm{sgn}(z_n(t))\right\} \\ &-\mu[N_0 + K\tan\gamma\phi_D\left|z_n(t)\right|]\phi_D\,\mathrm{sgn}(\dot{z}_n(t)), \end{aligned} \tag{8}$$

where the subscript "n" designates quantities corresponding to the nth assumed beam mode. (Note that, without loss of generality, use has been made of the assumption that $\phi_D = \phi_n(x_D) > 0$.)

Even for an unforced model described by a single beam mode, it is seen that the governing equation involves a large number of physical parameters. The equation can be simplified somewhat if one introduces the

following parameters:

$$k_1 = \frac{K\phi_D^2}{m_n\omega_n^2}, \quad n_0 = \frac{N_0\phi_D}{m_n\omega_n^2}, \quad \tau = \omega_n t\sqrt{1+k_1\tan^2\gamma}, \quad \eta = \frac{-\zeta_n}{\sqrt{1+k_1\tan^2\gamma}}$$
$$R = \frac{\tan\gamma}{\mu}, \quad \delta = \frac{\mu k_1\tan\gamma}{1+k_1\tan^2\gamma}, \quad f_0 = \frac{\mu n_0}{(1+k_1\tan^2\gamma)}. \tag{9}$$

Making use of Eq. (9) and noting that $|z_n|\,\mathrm{sgn}\,(z_n) = z_n$, the unforced Eq. (8) can be written as

$$z'' - 2\eta z' + z + \delta|z|\,\mathrm{sgn}(z') + f_0\,\mathrm{sgn}(z') + f_0 R\,\mathrm{sgn}(z) = 0, \tag{10}$$

where derivatives with respect to nondimensional time τ are denoted by a prime and the subscripts on $z(t)$ have been suppressed for simplicity. Note that since the primary concern of the present work is the stability and free response of the system under the influence of *negative viscous damping*, the sign of the viscous damping term has been negated in Eq. (10).

3. Analysis

3.1. Sticking criteria

Since system (10) is unforced and assumes a single beam mode to represent flexure, if sticking occurs, the beam will remain stuck for all subsequent times. As developed in Ref. [21], sticking is easily determined by examining the sign of the acceleration for very small velocities. Let $a^+ = z''$ for $z' = 0^+$ and let $a^- = z''$ for $z' = 0^-$:

$$a^+ = -(1+\delta)z - f_0 - f_0 R, \tag{11a}$$

$$a^- = -(1-\delta)z + f_0 - f_0 R. \tag{11b}$$

Consider a response trajectory that hits the z-axis with displacement z. If for this value of z, $a^+ \leqslant 0$ while $a^- \geqslant 0$, then the system will stick and remain stuck for all time after the first occurrence of zero velocity. Determination of the sticking range is simplified if one notes that $a^+ < 0$ for all positive z, and $a^- > 0$ for all negative z. Furthermore, the sticking ranges should be symmetric for positive and negative values of z.

The occurrence of sticking is critically dependent on two positive dimensionless constants, R and δ. The ratio R is important in static "wedge-type" problems, where $R<1$ is known to be necessary for sticking to occur. The parameter δ can be interpreted as a ratio of the friction force increase (above that due to the preload alone) to the total elastic restoring force. Although not readily apparent, the parameters R and δ are related by an inequality constraint:

$$R\delta = \frac{\tan\gamma}{\mu}\,\frac{\mu k_1\tan\gamma}{1+k_1\tan^2\gamma} = \frac{k_1\tan^2\gamma}{1+k_1\tan^2\gamma} < 1. \tag{12}$$

As long as this constraint is satisfied, it is always possible to find a set of physical system parameters (such as m, E, L, K, etc.) that give a particular set of dimensionless constants η, δ, R, and f_0. Depending on the values of R and δ, there are three sticking cases:

$$R<1 \text{ and } \delta<1 \Rightarrow \text{sticking occurs for } |z| < z_{\text{threshold}} = f_0\frac{1-R}{1-\delta}, \tag{13a}$$

$$R<1 \text{ and } \delta>1 \Rightarrow \text{sticking occurs for all } z, \tag{13b}$$

$$R>1 \text{ and } \delta<1 \Rightarrow \text{no sticking possible for any } z. \tag{13c}$$

The case where $R>1$ and $\delta>1$ is not physically possible due to inequality (12). However, for completeness, the corresponding sticking region would be

$$R>1 \text{ and } \delta>1 \Rightarrow \text{sticking occurs for } |z| > f_0\frac{1-R}{1-\delta}. \tag{13d}$$

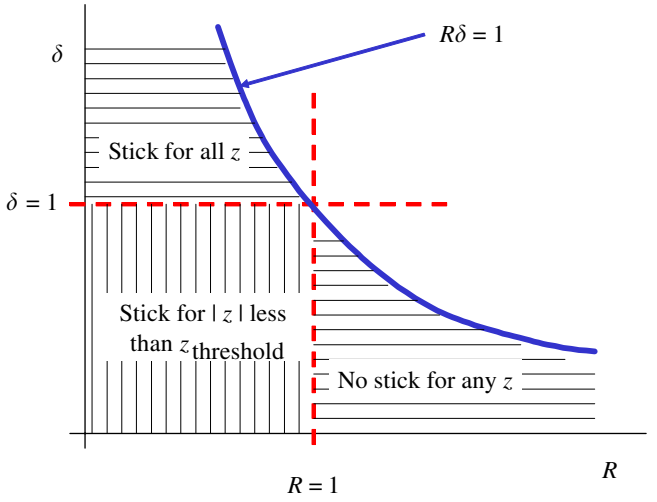

Fig. 2. Sticking regions in $R-\delta$ parameter space.

The regions are shown pictorially in Fig. 2. Starting near the origin in the $R-\delta$ parameter space, $z_{\text{threshold}}$ diminishes as R is increased. At $R=1$, the sticking threshold along the z-axis shrinks to zero. Conversely, starting near the origin in the $R-\delta$ parameter space, $z_{\text{threshold}}$ increases as δ is increased. At $\delta=1$, the sticking threshold grows to include the entire z-axis.

Not surprisingly, $R<1$ (i.e., $\mu>\tan\gamma$) is a necessary condition for sticking to be possible. Conversely, $\delta>1$ is a necessary condition for sticking at large displacements. It is also important to note that in the case of zero preload, $f_0=n_0=0$, the system sticks for all z when $\delta>1$ and remains stick-free otherwise.

3.2. Free response

An exact solution can be constructed starting from the initial conditions $z(0)=z_0>0$ and $z'(0)=0$. From this initial condition, the trajectory traverses the fourth quadrant where the linear governing equation can be written as

$$z''-2\eta z'+(1-\delta)z-f_0(1-R)=0. \tag{14}$$

As discussed above, the system remains stuck at $z=z_0$ if $\delta>1$. Therefore, we assume $\delta<1$ in the sequel. Using subscripts suggestive of the quadrant in which the equation applies, we can rewrite Eq. (14) in the form:

$$z''-2\zeta_4\Omega_4 z'+\Omega_4^2 z=\Omega_4^2 c_4, \tag{15}$$

where

$$\Omega_4^2=(1-\delta),\quad \zeta_4=\eta/\Omega_4,\quad \text{and}\quad c_4=f_0(1-R)/(1-\delta).$$

Note that c_4 has the same value as $z_{\text{threshold}}$, which appears in the definition of the sticking regions (13a). Assuming that $|\zeta_4|\neq 1$, the exact solution to this equation is given by

$$z(\tau)=\frac{\left(\lambda_1 e^{\lambda_2\tau}-\lambda_2 e^{\lambda_1\tau}\right)}{\lambda_1-\lambda_2}(z_0-c_4)+c_4, \tag{16}$$

$$z'(\tau)=\frac{(\lambda_1\lambda_2)}{\lambda_1-\lambda_2}\left(e^{\lambda_2\tau}-e^{\lambda_1\tau}\right)(z_0-c_4), \tag{17}$$

where

$$\lambda_1=\zeta_4\Omega_4-\Omega_4\sqrt{\zeta_4^2-1},\quad \lambda_2=\zeta_4\Omega_4+\Omega_4\sqrt{\zeta_4^2-1}. \tag{18a,b}$$

Note that Eqs. (16) and (17) apply to the case of real or complex values for λ_1 and λ_2; however, they do not apply to the case of critical damping, $|\zeta_4| = 1$, which results in real repeated roots, $\lambda = \lambda_1 = \lambda_2$. The solution in this case can be written as

$$z = (z_0 - c_4)(1 - \lambda\tau)e^{\lambda\tau} + c_4, \tag{19}$$

$$z' = -(z_0 - c_4)\lambda^2\tau e^{\lambda\tau}. \tag{20}$$

Given a particular initial displacement z_0, three possible scenarios can develop as shown in Fig. 3.

(1) The first scenario is that $z_0 < z_{\text{threshold}}$. In this case, no motion takes place.
(2) The second scenario is that the displacement decreases but never reaches zero before permanent sticking takes place. In this case, the trajectory begins by entering Quadrant IV, but terminates on the positive z-axis. See, for example, the case A in Fig. 3, with initial displacement equal to z_A.
(3) The third and more interesting scenario is that the trajectory passes through Quadrant IV and into Quadrant III. This is the situation pertaining to the initial displacement z_C in Fig. 3. Assume that the trajectory passes into the third quadrant when $\tau = \tau_1$, at which time $z(\tau_1) = 0$ and $z'(\tau_1) = v_1$. The determination of τ_1 requires the solution of a transcendental equation, namely the equation formed by setting the right-hand side of Eq. (16) equal to zero. (In the special case where c_4 is equal to zero, it is possible to obtain a closed-form solution for τ_1 and v_1. This case will be treated separately below.)

It is seen that there is a limiting value of z_0 such that reaching Quadrant III is ensured. This point, labeled as point z_B in Fig. 3, can be found in a closed form as follows. First, recognize that a trajectory originating at the point z_B on the $+z$-axis will terminate at the origin. Thus, we can utilize a time-reversed solution to Eq. (14). Define $p = \tau_1 - \tau$. Then the general solution to Eq. (14) can be written as

$$z(p) = Ae^{\lambda_1(\tau_1 - p)} + Be^{\lambda_2(\tau_1 - p)} + c_4 = \hat{A}e^{-\lambda_1 p} + \hat{B}e^{-\lambda_2 p} + c_4. \tag{21}$$

The (possibly) complex-valued undetermined constants $\hat{A}$ and $\hat{B}$ can be found by applying the initial conditions $z(p = 0) = 0$ and $dz(p = 0)/(dp) = 0$. This gives the solution

$$z(p) = \frac{c_4}{\lambda_1 - \lambda_2}\left(\lambda_2 e^{-\lambda_1 p} - \lambda_1 e^{-\lambda_2 p}\right) + c_4, \tag{22}$$

$$\frac{dz(p)}{dp} = \frac{c_4\lambda_1\lambda_2}{\lambda_1 - \lambda_2}\left(e^{-\lambda_2 p} - e^{-\lambda_1 p}\right). \tag{23}$$

Judging from Eq. (23), we see that in order for dz/dp to be zero for some $p > 0$, it is necessary that the roots be complex-valued; i.e., $|\zeta_4| < 1$. Let $\lambda_1 = -\zeta_4\Omega_4 - i\Omega_4\sqrt{1 - \zeta_4^2} = -\zeta_4\Omega_4 - i\omega_{d4} = \lambda_2^*$, where $\omega_{d4} = \Omega_4\sqrt{1 - \zeta_4^2}$ is the damped natural frequency in Quadrant IV. The first value of $p > 0$ for which the velocity equals zero is

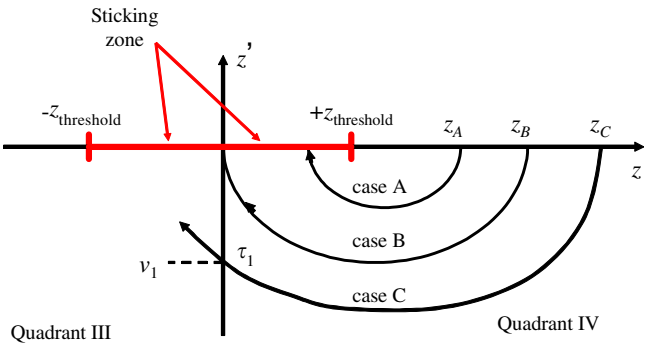

Fig. 3. Response possibilities in Quadrant IV.

simply $p_1 = \pi/\omega_{d4}$. The value of displacement at $p = p_1$ is given by

$$z_B = z(p_1) = \frac{c_4}{\lambda_1 - \lambda_2}\left(\lambda_2 e^{-\lambda_1 p_1} - \lambda_1 e^{-\lambda_2 p_1}\right) + c_4 = c_4\left(1 + e^{-\zeta_4 \Omega_4 \pi/\omega_{d4}}\right),$$

$$z_B = c_4\left(1 + e^{-\zeta_4 \pi/\sqrt{1-\zeta_4^2}}\right). \tag{24}$$

Note that as $\zeta_4 \to 1$, $z_B \to c_4$. For $\zeta_4 > 1$, the point ($z_{\text{threshold}}$, 0) takes on the characteristics of an unstable node, with trajectories slowly approaching it as $\tau \to -\infty$.

For $z_0 > z_B$, the trajectory is guaranteed to reach the third quadrant at some time τ_1, having zero displacement and having a velocity of v_1. Once in the third quadrant, the following governing equation applies:

$$z'' - 2\eta z' + (1+\delta)z - f_0(1+R) = 0, \quad \tau > \tau_1. \tag{25}$$

As before, we introduce the following notation to simplify the form of the solution:

$$\Omega_3^2 = (1+\delta), \quad \zeta_3 = \eta/\Omega_3, \quad \text{and} \quad c_3 = f_0(1+R)/(1+\delta).$$

This yields

$$z'' - 2\zeta_3 \Omega_3 z' + \Omega_3^2 z = \Omega_3^2 c_3. \tag{26}$$

Assuming that $|\zeta_3| \neq 1$, the general solution to Eq. (26) can be written as

$$z(\tau) = \frac{1}{\sigma_4 - \sigma_3}\left\{-(v_1 + c_3\sigma_4)e^{\sigma_3(\tau-\tau_1)} + (v_1 + c_3\sigma_3)e^{\sigma_4(\tau-\tau_1)}\right\} + c_3, \tag{27}$$

$$z'(\tau) = \frac{1}{\sigma_4 - \sigma_3}\left\{-\sigma_3(v_1 + c_3\sigma_4)e^{\sigma_3(\tau-\tau_1)} + \sigma_4(v_1 + c_3\sigma_3)e^{\sigma_4(\tau-\tau_1)}\right\}, \tag{28}$$

where

$$\sigma_3 = \zeta_3\Omega_3 - \Omega_3\sqrt{\zeta_3^2 - 1} \quad \text{and} \quad \sigma_4 = \zeta_3\Omega_3 + \Omega_3\sqrt{\zeta_3^2 - 1}. \tag{29a,b}$$

It should be noted that, as for the solution presented above for Quadrant IV, the form given in Eqs. (27) and (28) hold for both the case of complex roots and the case of real-distinct roots. In the case $|\zeta_3| = 1$, $\sigma = \sigma_3 = \sigma_4$, the critical-damping solution is required:

$$z = c_3(1 - e^{\sigma(\tau-\tau_1)}) + (v_1 + c_3\sigma)(\tau - \tau_1)e^{\sigma(\tau-\tau_1)}, \tag{30}$$

$$z' = \left\{v_1 + \sigma(v_1 + c_3\sigma)(\tau - \tau_1)\right\}e^{\sigma(\tau-\tau_1)}. \tag{31}$$

The time at which the trajectory moves into Quadrant II can be determined by setting (28) equal to zero. Denoting this time as τ_2, one finds after some manipulation:

$$\tau_2 = \tau_1 + \frac{\ln\left((\sigma_3(v_1 + c_3\sigma_4))/(\sigma_4(v_1 + c_3\sigma_3))\right)}{\sigma_4 - \sigma_3}. \tag{32}$$

Note that care must be taken to ensure that a real-valued result for τ_2 exists and that it is greater than τ_1. If σ_3 and σ_4 are complex-valued, the magnitude of the imaginary parts of σ_3 and σ_4 can be identified as the damped natural frequency in Quadrant III, ω_{d3}. The corresponding damped natural period would thus be given by $T_{d3} = 2\pi/\omega_{d3}$ and the solutions of Eq. (32) are separated by a time interval equal to $T_{d3}/2$:

$$\Delta\tau = \frac{T_{d3}}{2} = \frac{\pi}{\omega_{d3}} = \frac{\pi}{\Omega_3\sqrt{1-\zeta_3^2}}. \tag{33}$$

Therefore, it may be necessary to add multiples of $\Delta\tau$ to the numerical value found by means of expression (32) until a value of τ_2 is found that is greater than τ_1. If σ_4 and σ_3 are real-valued and distinct, the situation is more involved. Note from Eq. (29) above that if $\zeta_3 > 1$, the real roots will be ordered so that $\sigma_4 > \sigma_3 > 0$. An inspection of Eq. (28) shows that the velocity will become positive if and only if the coefficient of $e^{\sigma_4(\tau-\tau_1)}$ is

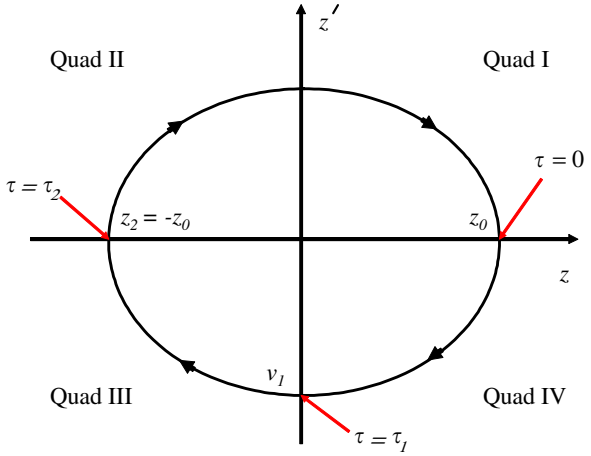

Fig. 4. Bounding orbit surrounding stable region.

positive. Thus, unless $(v_1 + c_3\sigma_3) > 0$, the trajectory will remain in Quadrant III with increasingly negative velocity as τ goes to infinity. It can be shown that the same condition applies for the case of $|\zeta_3| = 1$.

Provided that v_1 and τ_2 exist, the corresponding displacement, denoted z_2, may be obtained by evaluating Eq. (27) or Eq. (30) at $\tau = \tau_2$. The mapping from $z_0 > 0$ to $z_2 < 0$ may be considered to be a nonlinear function of the starting value:

$$z_2 = P(z_0). \tag{34}$$

Due to the fact that the piecewise-linear system dynamics in Quadrants II and I are identical to those in Quadrants IV and III, respectively, it is clear that the mapping P can also be used in the upper half of the phase plane; i.e., mapping displacements on the negative z-axis onto displacements on the positive z-axis. When $z_2/z0 < -1$, the amplitude of the oscillations grows with time. When $z_2/z_0 > -1$, the amplitude of the oscillations decreases with time. The case where $z_2/z_0 = -1$ is shown in Fig. 4. In this case, the trajectory oscillates indefinitely with period $T = 2\tau_2$. The closed orbit separates the phase plane into an interior region within which trajectories are attracted to a zone of equilibria on the z-axis given by the sticking relations (13). In the case where no sticking is possible ($R > 1$), the origin becomes a stable attractor for all trajectories originating within the bounding orbit. Trajectories originating outside of the bounding orbit will grow unbounded with time unless or until they intersect the z-axis in one of the sticking regions given in Eqs. (13). Note that the equilibrium orbit is an unstable limit cycle. Thus, a relatively easy way to check its size and shape is by integrating the original differential equation (10) backwards in time. Alternatively, an approximate solution may be sought using the harmonic-balance (HB) procedure.

3.3. Harmonic balance

Since Eq. (10) is autonomous, we can assume a solution for displacement of the form $z = Z\cos(\omega\tau)$. It can be shown that the fundamental-frequency approximations of the nonlinear terms of Eq. (10) are given by

$$\operatorname{sgn}(Z\cos(\omega\tau)) \approx (4/\pi)\cos(\omega\tau), \quad \operatorname{sgn}(-Z\omega\sin(\omega\tau)) \approx -(4/\pi)\sin(\omega\tau), \tag{35a,b}$$

$$|Z\cos(\omega\tau)|\operatorname{sgn}(-Z\omega\sin(\omega\tau)) \approx -(2/\pi)Z\sin(\omega\tau). \tag{35c}$$

Note that these approximations assume $Z > 0$ and $\omega > 0$. Using the harmonic approximation for $z(\tau)$ and its derivatives as well as the approximations in Eq. (35), we can equate the cosine and sine components in Eq. (10) separately. Balancing the terms involving $\cos(\omega\tau)$ yields:

$$-Z\omega^2 + Z + (4/\pi)f_0 R = 0. \tag{36}$$

Balancing the terms involving $\sin(\omega\tau)$, we obtain:

$$+2\eta\omega Z - (2/\pi)\delta Z - (4/\pi)f_0 = 0. \tag{37}$$

The frequency ω can be eliminated between the two equations, yielding a quadratic equation for the amplitude Z:

$$aZ^2 + bZ + c = 0, \tag{38}$$

where

$$a = 4\left(\eta^2 - (\delta/\pi)^2\right), \quad b = \left(16f_0/\pi\right)\left(R\eta^2 - \delta/\pi\right), \quad \text{and } c = -(4f_0/\pi)^2. \tag{39a,b,c}$$

The fact that $c<0$ can be used to determine the conditions under which positive solutions to Eq. (38) are possible. If $a \geqslant 0$, the quadratic equation will always have one positive real root and one negative real root, regardless of the value of b. [Note that the situation of $a = b = 0$ results in an inconsistency.] When $a<0$, the roots to Eq. (38) are complex-valued unless $b^2 > 4ac$; i.e.,

$$\left(16f_0/\pi\right)^2\left(R\eta^2 - \delta/\pi\right)^2 > 4\cdot 4\left(\eta^2 - (\delta/\pi)^2\right)\cdot(4f_0/\pi)^2. \tag{39}$$

For $f_0 \neq 0$, this implies

$$\left(R\eta^2 - \delta/\pi\right)^2 > \left(\eta^2 - (\delta/\pi)^2\right) \Rightarrow R^2\eta^4 - \left(2R\delta/\pi - 1\right)\eta^2 > 0 \quad \text{or} \quad R^2\eta^2 > \left(2R\delta/\pi - 1\right). \tag{40}$$

By inequality (12), however, $R\delta<1$, so the situation of $b^2>4ac$ is not physically possible in the case $a<0$. As $a \to 0^+$, the positive root of Eq. (38) tends to infinity. Thus, as $\delta/\pi \to \eta$, the amplitude of the bounding orbit should approach infinity, which implies *global stability*.

3.4. Zero-preload case

In the special case where n_0 is zero, the analysis above can be simplified considerably. Note that if $n_0 = 0$, then $c_3 = c_4 = 0$ in the expressions above. The first consequence of this situation may be seen in the sticking conditions (13). With $n_0 = 0$, the sticking conditions depend only on δ; if $\delta<1$, no sticking is possible along the z-axis and if $\delta>1$, sticking will occur everywhere along the z-axis.

With $c_4 = 0$, it is possible to find a closed-form solution for τ_1. For the case of $|\zeta_4| \neq 1$, τ_1 is given by

$$\tau_1 = \frac{\ln\left(\lambda_1/\lambda_2\right)}{\lambda_1 - \lambda_2}. \tag{41}$$

As before, in the case of $|\zeta_4|<1$ it may be necessary to adjust the obtained value of τ_1 by adding multiples of $T_{d4}/2 = \pi/(2{*}\text{imag}(\lambda_2))$ until a positive value of τ_1 is obtained. When $|\zeta_4| = 1$, Eq. (19) reveals that $\tau_1 = 1/\sqrt{1-\delta}$. With $c_4 = 0$, Eq. (17) or Eq. (20) shows that v_1 is a linear function of z_0 of the form

$$v_1 = L_4 z_0, \tag{42}$$

where L_4 is the linear mapping from the $+z$-axis to the $-z'$-axis through Quadrant IV. For $|\zeta_4| \neq 1$, it is given by

$$L_4 = \frac{(\lambda_1\lambda_2)}{\lambda_1 - \lambda_2}\left(e^{\lambda_2\tau_1} - e^{\lambda_1\tau_1}\right). \tag{43}$$

Eq. (24) shows that $z_B = 0$ which implies that all trajectories originating on the $+z$-axis are guaranteed to enter Quadrant III. The time τ_2 at which the trajectories leave Quadrant III is still given by Eq. (32). With $c_3 = 0$, Eq. (32) simplifies to

$$\tau_2 = \tau_1 + \frac{\ln\left(\sigma_3/\sigma_4\right)}{\sigma_4 - \sigma_3}. \tag{44}$$

Referring to Eq. (29a,b), it is seen that in the case of $|\zeta_3| \geqslant 1$, σ_3 and σ_4 are real-valued and ordered so that $\sigma_4 \geqslant \sigma_3$. Therefore, no real value of $\tau_2 > \tau_1$ will exist unless $|\zeta_3|<1$. (Recall that, even for the underdamped

case, it may be necessary to add multiples of $T_{d3}/2$ to the value obtained from Eq. (44) in order to render a value of $\tau_2 > \tau_1$.)

Inspection of Eqs. (27) and (30) above with $c_3 = 0$ shows that z_2 is a linear function of v_1 of the form

$$z_2 = L_3 v_1, \tag{45}$$

where L_3 is the linear mapping from the $-z'$-axis to the $-z$-axis through Quadrant III. For the case $|\zeta_3| \neq 1$, L_3 is given by

$$L_3 = \frac{1}{\sigma_4 - \sigma_3}\left\{e^{\sigma_4(\tau_2-\tau_1)} - e^{\sigma_3(\tau_2-\tau_1)}\right\}. \tag{46}$$

Combining (43) and (46), the mapping from z_0 to z_2 is obtained as

$$z_2 = Pz_0 = L_3 L_4 z_0. \tag{47}$$

Due to the linearity of expression (47), it may be concluded that the stability of the phase-plane origin is not dependent on the system's initial state. If $L_3L_4 < -1$, trajectories grow without bound regardless of initial displacement z_0. Conversely, if $L_3L_4 > -1$, trajectories diminish with time regardless of initial displacement z_0. If $L_3L_4 = -1$, the origin takes on the characteristics of a center, with all values of z_0 giving rise to closed orbits. This type of behavior is also evident in the HB solutions (36) and (37). When $f_0 = 0$, Eqs. (36) and (37) have no solution unless $\omega = 1$ and $\eta = \delta/\pi$. If these two conditions are met, the value of Z is arbitrary, consistent with the attributes of a center.

In the general case of zero preload, it is seen that L_3L_4 depends only on the values of η and δ. Thus, the $\eta-\delta$ parameter space can be partitioned into regions of instability ($L_3L_4 < -1$) and regions of stability ($L_3L_4 > -1$). Fig. 5 shows the boundary between these two regions, where $L_3L_4 = -1$. Along this line, the system exhibits center-type stability while combinations of η and δ below this curve give rise to globally asymptotic stability. For comparison, the HB requirement for a center, $\eta = \delta/\pi$, is also shown. Note that there is a very good agreement between the HB prediction and the exact solution except for relatively large values of δ. This is to be expected since, with $f_0 = 0$, δ alone determines the size of the nonlinear term in Eq. (10).

As a further simplification, we can consider the case where the viscous damping term is identically zero. Then, expression (47) reduces to

$$\frac{z_2}{z_0} = \sqrt{\frac{1-\delta}{1+\delta}}. \tag{48}$$

Over a full cycle, the ratio of amplitudes is the square of the right-hand side, $(1-\delta)/(1+\delta)$, which matches the results of Caughey and Vijayaraghavan [10] and Inaudi et al. [20]. This ratio of amplitudes can be used to

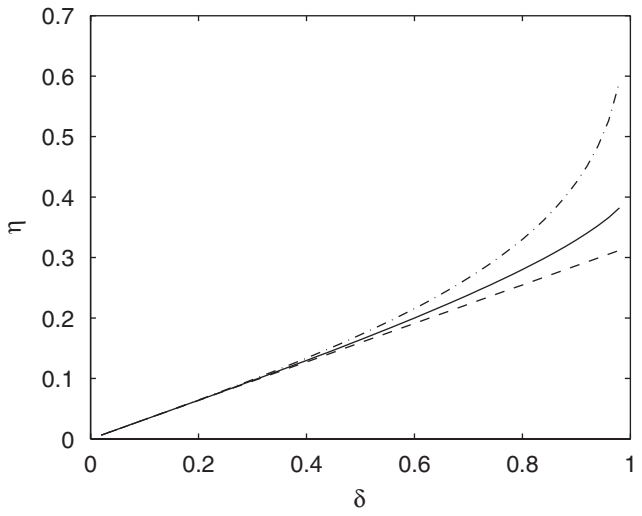

Fig. 5. Stability diagram in $\eta-\delta$ parameter space. Solid line, exact boundary; dashed line, harmonic balance; dash–dot line, log decrement.

determine an *equivalent viscous damping ratio* based on the log-decrement approach. Let $(z)_i$ be the peak amplitude over the ith cycle of decaying response. Then

$$\ln\left(\frac{(z)_i}{(z)_{i+1}}\right) = \ln\left(\frac{1+\delta}{1-\delta}\right) = \Delta = \frac{2\pi\,\zeta_d}{\sqrt{1-\zeta_d^2}} \Rightarrow \quad \zeta_d = \frac{\Delta}{\sqrt{4\pi^2+\Delta^2}}, \tag{49}$$

where ζ_d is the equivalent viscous damping ratio based on matching the log-decrement of the friction-damped system with that of a linear, underdamped single-degree-of-freedom system. Presumably, if $\zeta_d > \eta$, the system should be stable; the boundary where $\zeta_d = \eta$ could thus be used to form another boundary line in the $\eta-\delta$ parameter space. As seen in Fig. 5, this result is in excellent agreement with the exact solution and with the HB result for small values of δ. However, as δ increases, the three results diverge. Over the entire range of δ, the HB result yields a conservative estimate of the stable region in the $\eta-\delta$ parameter space while the log-decrement approach overpredicts the stable region.

4. Results

The size and shape of the bounding orbit is highly dependent on the system parameters. Interestingly, the influence of f_0 on the amplitude of the bounding orbit z_0 is purely linear. This can be justified by an examination of Eq. (10). Let $\tilde{z}(\tau)$ be a bounding-orbit solution to Eq. (10) with starting displacement $\tilde{z}(0) = \tilde{z}_0$. Then

$$\tilde{z}'' - 2\eta\,\tilde{z}' + \tilde{z} + \delta|\tilde{z}|\mathrm{sgn}(\tilde{z}') + f_0\,\mathrm{sgn}(\tilde{z}') + f_0 R\,\mathrm{sgn}(\tilde{z}) = 0. \tag{50}$$

It is obvious that $\alpha\tilde{z}(\tau)$ satisfies the same equation with f_0 replaced with αf_0. Thus, the effect of f_0 is to increase the amplitude of the bounding orbit by a simple scale factor. For this reason, one need only consider two values of f_0: $f_0 = 0$ and $f_0 = 1$.

Fig. 6 shows the bounding orbits for three different values of δ. As δ gets larger, the size of the bounding orbit gets larger but becomes perceptibly less elliptical in shape. For $\delta = 0.1$, the bounding orbit as derived using the exact solution is compared against the HB prediction in Fig. 7. The good agreement between the HB and exact solutions attests to the fact that for small-sized orbits (small stable regions), the exact solution is well-approximated by an elliptical approximation such as HB. Fig. 8 shows the HB and exact solutions compared over a single cycle of motion. While the phase of the HB solution is arbitrary, the figure still demonstrates that there is a noticeable difference in the periods predicted by the two methods.

Fig. 9 shows a similar comparison for $\delta = 0.6$. With the larger-sized bounding orbit, there is a very large discrepancy between the HB and exact solutions.

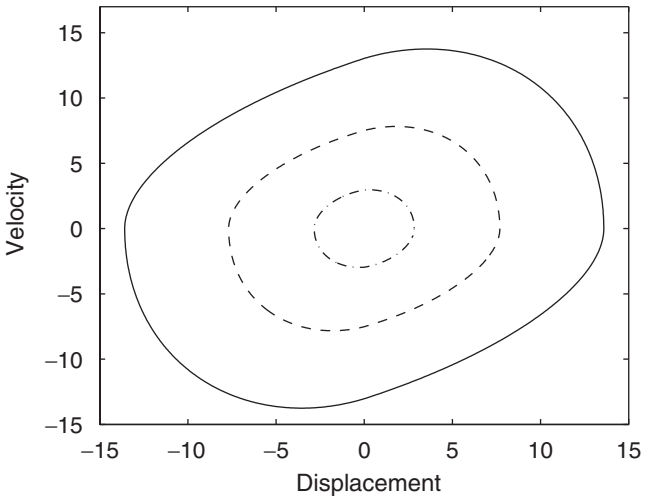

Fig. 6. Bounding orbits for various values of δ; $\eta = 0.25$, $R = 0.2$, $f_0 = 1$. Solid line, $\delta = 0.6$; dashed line, $\delta = 0.5$; dash–dot line, $\delta = 0.1$.

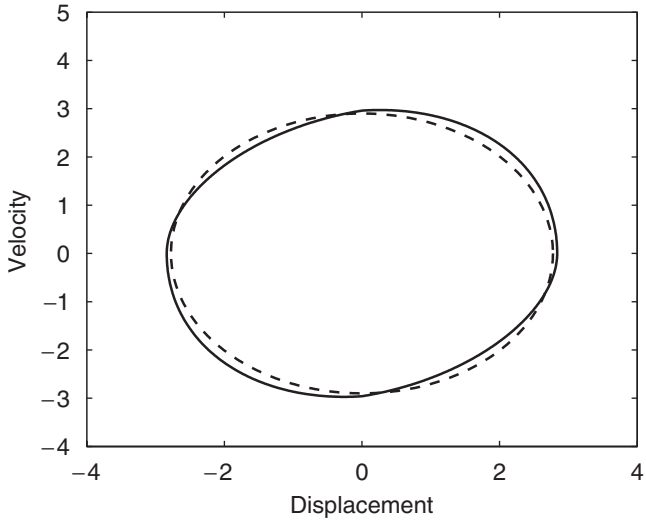

Fig. 7. Comparison of bounding orbit calculated using the exact solution and the harmonic-balance method. $\delta = 0.1$, $\eta = 0.25$, $R = 0.2$, $f_0 = 1$. Solid line, exact; dashed line, harmonic balance.

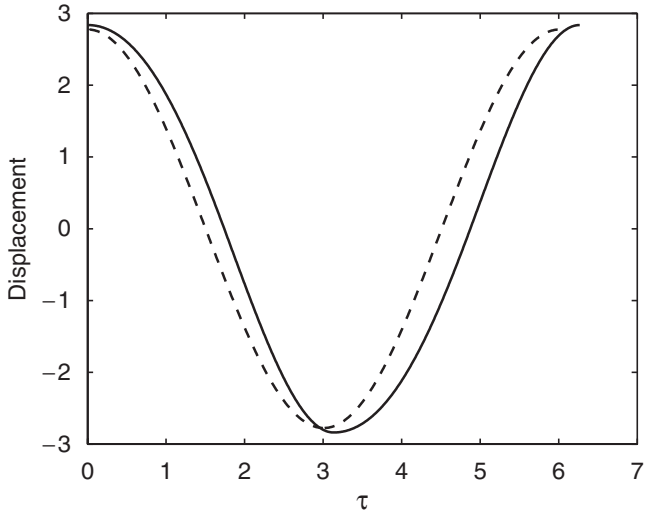

Fig. 8. Comparison of bounding orbit predictions in the time domain. $\delta = 0.1$, $\eta = 0.25$, $R = 0.2$, $f_0 = 1$. Solid line, exact; dashed line, harmonic balance.

The dependence of the bounding-orbit amplitude with δ is shown in Fig. 10 for $\eta = 0.1$, $R = 0.2$, and $f_0 = 1$. Also shown in the figure is the HB prediction, which is fairly good. It is seen that the size of the stable region increases with δ-first gradually and then very sharply. In fact, for $\delta = 0.3107$, the solution is infinite, and for $\delta > 0.3107$, no solution for z_0 exists. This curious fact can be explained by referring to the solution obtained for the zero-preload case, $n_0 = f_0 = 0$. As the amplitude of the bounding solution becomes larger and larger, the relative influence of the preload terms in Eq. (10) becomes smaller and smaller. In the limit of an infinite-amplitude orbit, the f_0 terms in Eq. (10) can be discarded with the resulting system being identical to that governed by the zero-preload case. As Fig. 5 shows, a zero-preload system with $\eta = 0.1$ is unstable for $\delta < 0.3107$; at $\delta = 0.3107$, the origin becomes a neutrally stable center. For $0.3107 < \delta < 1$, the zero-preload

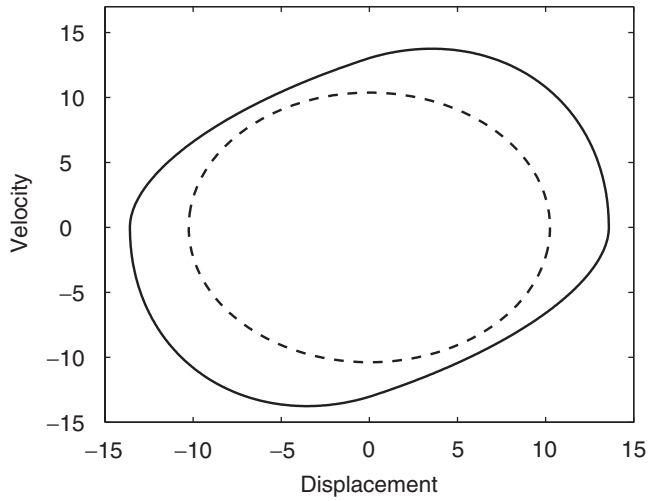

Fig. 9. Comparison of bounding orbit calculated using the exact solution and the harmonic-balance method. $\delta = 0.6$, $\eta = 0.25$, $R = 0.2$, $f_0 = 1$. Solid line, exact; dashed line, harmonic balance.

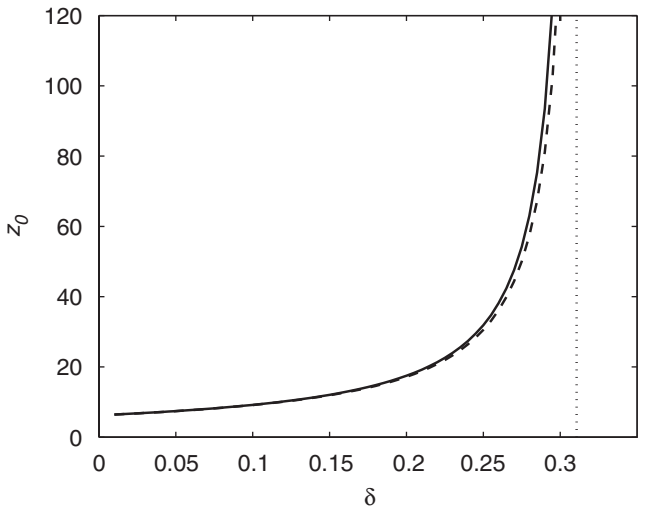

Fig. 10. Dependence of bounding-orbit amplitude vs. δ. $\eta = 0.1$, $R = 0.2$, $f_0 = 1$. Solid line, exact; dashed line, harmonic balance. The vertical line at $\delta = 0.3107$ denotes the limiting value of δ, beyond which no limit cycles exist.

system is globally asymptotically stable. For the system with nonzero preload, the unstable limit cycle disappears for $\delta > 0.3107$ and the system becomes globally stable, but not asymptotically so. Instead, the system is *ultimately bounded*, with trajectories terminating somewhere along the z-axis between $-z_{\text{threshold}}$ and $+z_{\text{threshold}}$. A similar result is found for the case of higher negative viscous damping, $\eta = 0.25$. As seen in Fig. 11, the amplitude of the bounding orbit increases sharply as δ approaches 0.7. At $\delta = 0.7293$, which corresponds exactly to the point in Fig. 5 for $\eta = 0.25$, the amplitude is infinite. Fig. 11 also shows that as δ increases, the agreement between the HB prediction and the exact solution deteriorates. As noted above, the HB solution predicts an infinite-amplitude bounding orbit when a in Eq. (38) is zero. This occurs at $\delta = \pi\eta = 0.7854$. Since in reality the system attains global stability at $\delta = 0.7293$, the HB prediction is conservative.

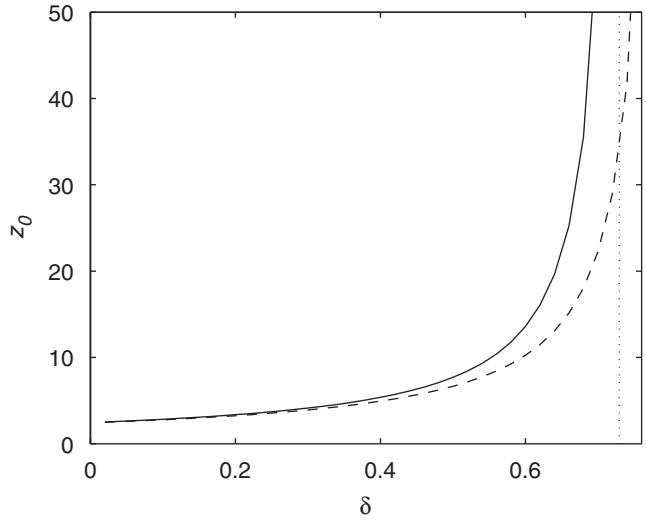

Fig. 11. Dependence of bounding-orbit amplitude vs. δ. $\eta = 0.25$, $R = 0.2$, $f_0 = 1$. Solid line, exact; dashed line, harmonic balance. The vertical line at $\delta = 0.7293$ denotes the limiting value of δ, beyond which no limit cycles exist.

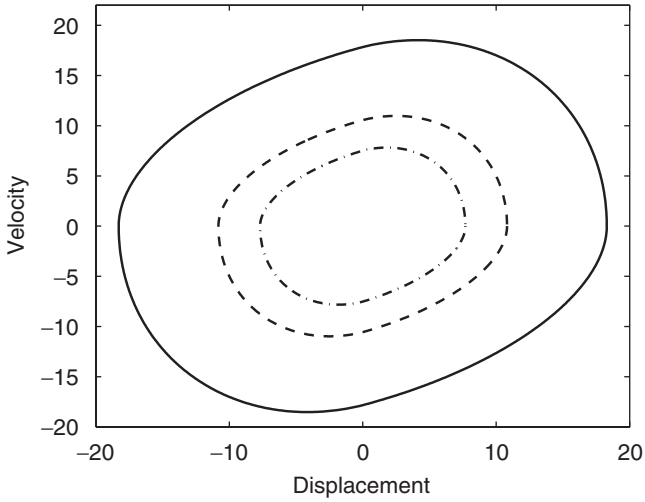

Fig. 12. Bounding orbits for various values of η; $\delta = 0.5$, $R = 0.2$, $f_0 = 1$. Solid line, $\eta = 0.2$; dashed line, $\eta = 0.225$; dash–dot line, $\eta = 0.25$.

The influence of η on the size and shape of the bounding orbit is shown in Figs. 12–14. As η is increased, the system becomes less stable; therefore, the amplitude of the bounding orbit for the stable region decreases. As η decreases, Fig. 13 shows that the amplitude of the bounding orbit rises asymptotically to infinity. For $\delta = 0.5$, Fig. 5 shows that the zero-preload system has neutral stability at $\eta = 0.1641$. By contrast, the HB result predicts $\eta = \delta/\pi = 0.1592$. As η increases, the amplitude of the bounding orbit gets smaller and smaller. However, for $z_0 < z_{\text{threshold}}$, no solution can be found for the bounding orbit because the trajectory commences from a terminally stuck position. In this case, $z_{\text{threshold}}$ is equal to $f_0(1-R)/(1-\delta) = 1.6$ and $z_0 = z_{\text{threshold}}$ at $\eta = 0.71$. Fig. 14 shows a bounding orbit for $\eta = 0.6$. It is seen that the shape of the orbit becomes very distorted as the amplitude approaches the limiting value of $z_{\text{threshold}} = 1.6$. For $\eta = 0.8$, no bounding orbit exists. However, as seen in Fig. 14, a domain of attraction for the sticking zone still exists. The boundary of the domain is found by using time-reversed solutions starting from the edges of the sticking zone.

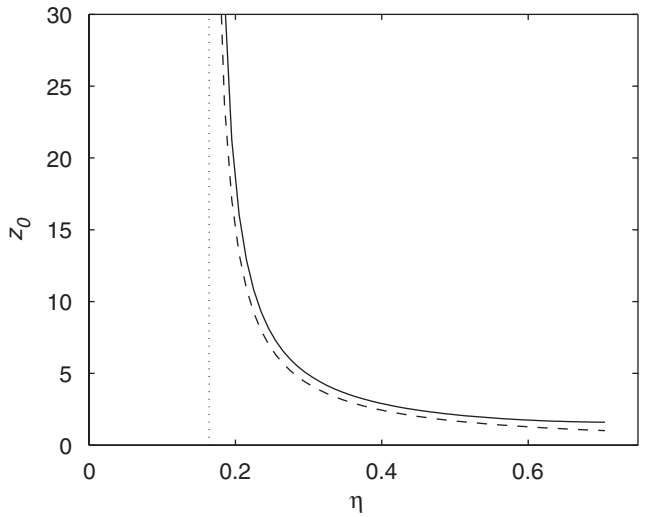

Fig. 13. Dependence of bounding-orbit amplitude on η. $\delta = 0.25$, $R = 0.2$, $f_0 = 1$. Solid line, exact; dashed line, harmonic balance. The vertical line at $\eta = 0.1641$ denotes the limiting value of η, below which no limit cycles exist.

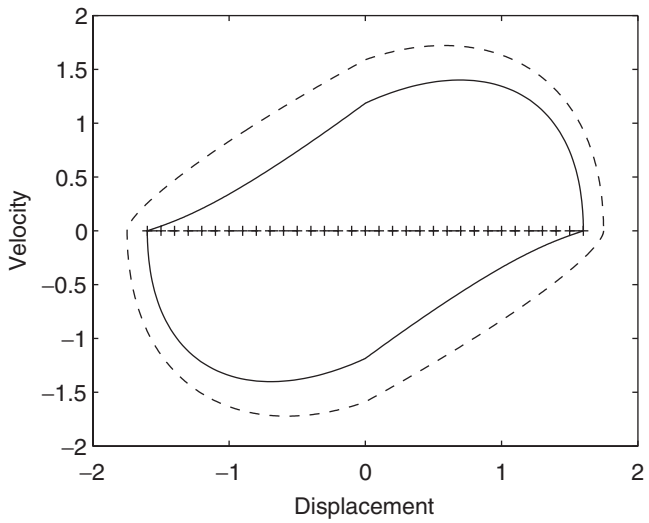

Fig. 14. Stability region for $\eta = 0.6$ (dashed) and $\eta = 0.8$ (solid). Sticking zone (plus signs) extends from -1.6 to $+1.6$ along the z-axis; $\delta = 0.5$, $R = 0.2$, $f_0 = 1$.

The dependence of the bounding-orbit amplitude on R is shown in Fig. 15. It is seen that the relationship is nearly linear, but is not exactly so. It should be noted that the maximum value of R is limited by the value of δ as discussed in relation to Eq. (12). Thus, $R < 1/\delta = 2$. It is seen that as R increases, the system becomes less stable. This would tend to suggest that increasing the ramp angle γ would have a *destabilizing effect on the system*. However, as shown below, this is not so.

While the introduction of the dimensionless constants aids in the derivation of general solutions, it obscures the role of certain physical parameters such as γ. To determine the influence of γ on the system stability, we consider a physical system with parameters similar to those used in earlier studies [4,5]. From the parameter values listed in Table 1, the following dimensionless constants are derived: $k_1 = 2.7019$, $n_0 = 1.0790$, $\mu = 0.5$, $\zeta_1 = -0.1$. As γ changes, the values of η, δ, R, and and f_0 will all change as shown in Fig. 16. It is seen that R and δ are strongly dependent on γ whereas η and f_0 are relatively constant.

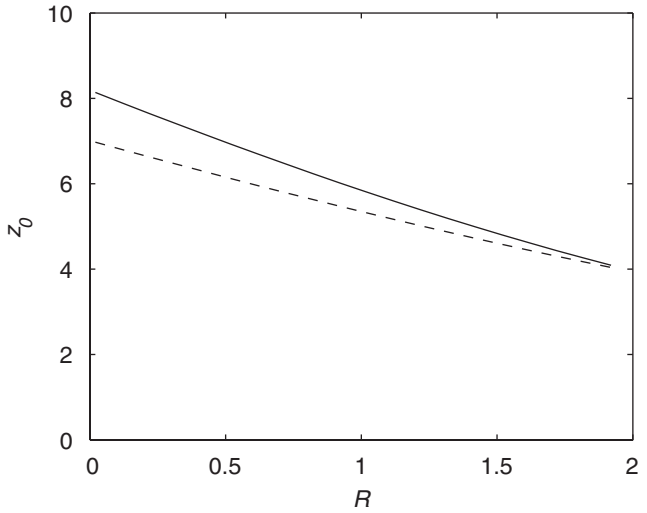

Fig. 15. Dependence of bounding-orbit amplitude on R. $\delta = 0.5$, $\eta = 0.25$, $f_0 = 1$. Solid line, exact; dashed line, harmonic balance.

Table 1
Physical parameters and derived constants

Symbol	Numerical value	Units
m	0.6361	kg/m
E	7.30E + 10	N/m^2
I	1.33E−10	m^4
L	0.3	m
N_0	10,000	N
ζ_1	−0.1	
K	10,000	N/m
μ	0.5	
x_D	0.2	m
m_1	1	kg
ϕ_D	2.504	
ω_1	152.3	rad/s

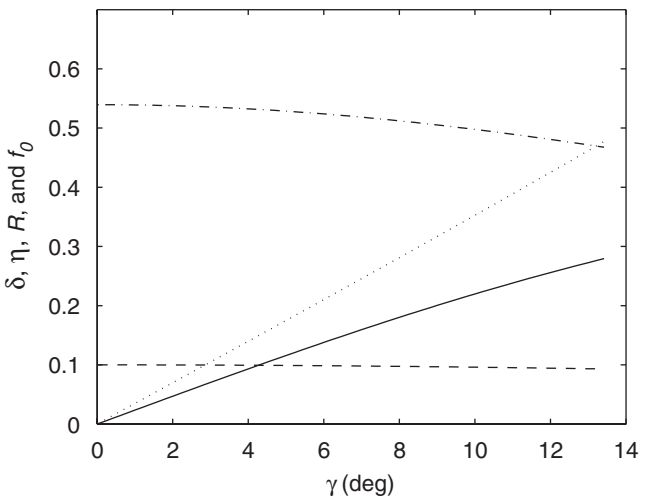

Fig. 16. Variation of dimensionless constants with ramp angle γ for $k_1 = 2.7019$, $n_0 = 1.0790$, $\mu = 0.5$, $\zeta_1 = -0.1$. Solid line, δ; dashed line, η; dash–dot line, f_0; dotted line, R.

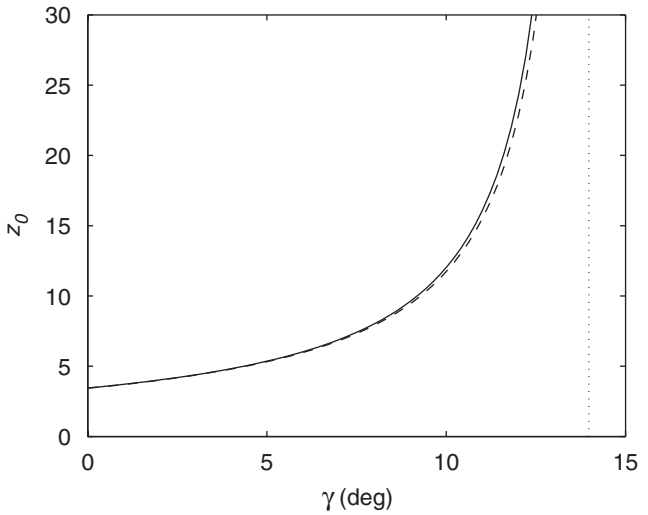

Fig. 17. Dependence of bounding-orbit amplitude on ramp angle γ. Solid line, exact; dashed line, harmonic balance. The vertical line at $\gamma = 13.9770^\circ$ denotes the limiting value of γ, above which no limit cycles exist.

Fig. 17 shows the variation of the bounding-orbit amplitude on ramp angle γ. It is clearly seen that the effect of γ is similar to that of δ; i.e., as γ increases, the system becomes more stable as evidenced by larger bounding orbits. Again, the presence of a finite value of γ at which the amplitude of the bounding orbit goes to infinity is observed. Beyond $\gamma = 13.9770^\circ$, the system is globally stable.

5. Conclusions

The free response and stability of a beam-like structure with a displacement-dependent dry friction damper attached was studied. Negative viscous damping was used to simulate destabilizing aerodynamic forcing, but the system was otherwise unforced. Using an exact solution for the piecewise-linear system, the conditions under which the dry friction forces could stabilize the system were determined. The results show that energy losses from the displacement-dependent dry friction damper can be large enough to overcome the destabilizing effects of negative viscous damping under certain conditions.

It was found that there is a significant qualitative difference between systems without preload and systems with preload across the frictional interface. The zero-preload case results in a homogeneous system whose stability is completely characterized by two parameters: η and δ. A stability diagram in $\eta-\delta$ parameter space was constructed to identify combinations of η and δ that led to stable, unstable, and neutrally stable behavior. Along the boundary, the origin takes on the characteristics of a center. The boundary of the stable and unstable domains obtained using an exact analysis was compared against an approximate result from HB and one obtained using a log-decrement damping approach. It was found that the two approximate techniques bounded the exact solution, with the HB result being more conservative. It was found that when the negative viscous damping is sufficiently low, global stability can be attained through the proper selection of the dry friction damper parameters.

In the case of systems with preload acting across the frictional interface, it was possible in most cases to create a region surrounding the origin in which all initial conditions gave rise to bounded response. In general, the trajectories originating in the stable domain terminated in a sticking zone containing the origin; in special cases, this zone of equilibria disappears and the origin becomes locally asymptotically stable. Surrounding this stable domain, an unstable limit cycle exists forming a bounding orbit; initial conditions chosen outside of this bounding orbit give rise to unbounded response. The influence of various system parameters on the size and shape of the bounding orbit was investigated. It was found that for certain values of the system parameters,

the amplitude of the bounding orbit became infinite, implying globally stable behavior. The exact conditions under which this occurs were derived using the zero-preload solution.

Acknowledgments

The authors would like to thank Dr. Philip M. FitzSimons, for his helpful suggestions. The first author also wishes to acknowledge National Science Foundation Grant No. CMS-0101122, which partially supported this work.

References

[1] K.E. Beucke, J.M. Kelly, Equivalent linearizations for practical hysteretic systems, *International Journal of Non-Linear Mechanics* 23 (4) (1985) 211–238.
[2] J.R. Anderson, A.A. Ferri, Behavior of a single-degree-of-freedom system with a generalized friction law, *Journal of Sound and Vibration* 140 (2) (1990) 287–304.
[3] N. Makris, M.C. Constantinou, Analysis of motion resisted by friction. I. Constant Coulomb and linear/Coulomb friction, *Mechanics of Structures and Machines* 19 (4) (1991) 477–500.
[4] W.E. Whiteman, A.A. Ferri, Displacement-dependent dry friction damping of a beam-like structure, *Journal of Sound and Vibration* 198 (3) (1996) 313–329.
[5] W.E. Whiteman, A.A. Ferri, Multi-mode analysis of beam-like structures subjected to displacement-dependent dry friction damping, *Journal of Sound and Vibration* 207 (3) (1997) 403–418.
[6] A.A. Ferri, Damping through use of passive and semi-active dry friction forces, in: A. Guran, F. Pfeiffer, K. Popp (Eds.), *Dynamics with Friction: Modeling, Analysis, and Experiment, Part II, Vol. 7, Series on Stability, Vibration, and Control of Structures*, World Scientific Publishing, Singapore, 2001, pp. 253–308.
[7] A. Sinha, J.H. Griffin, Friction damping of flutter in gas turbine engine airfoils, *AIAA Journal of Aircraft* 20 (4) (1983) 372–376.
[8] A.A. Ferri, E.H. Dowell, The behavior of a linear, damped modal system with a non-linear spring-mass-dry friction damper system attached, part II, *Journal of Sound and Vibration* 101 (1985) 55–74.
[9] S.H. Crandall, The role of structural damping in vibration theory, *Journal of Sound and Vibration* 11 (1) (1970) 3–18.
[10] T.K. Caughey, A. Vijayaraghavan, Free and forced oscillations of a dynamic system with 'linear hysteretic damping' (non-linear theory), *International Journal of Non-Linear Mechanics* 5 (3) (1970) 533–555.
[11] C.W. Bert, Material damping: an introductory review of mathematical models, measures and experimental techniques, *Journal of Sound and Vibration* 29 (2) (1973) 129–153.
[12] E.H. Dowell, H.C. Curtiss Jr., R.H. Scanlan, F. Sisto, *A Modern Course in Aeroelasticity*, Sijthoff and Noordhoff, Alphen aan den Rijn, The Netherlands, 1980.
[13] R.L. Bisplinghoff, H. Ashley, *Principles of Aeroelasticity*, Dover Publications, New York, 1962.
[14] A. Sinha, J.H. Griffin, R.E. Kielb, Influence of friction dampers on torsional blade flutter, *ASME Journal of Engineering for Gas Turbines and Power* 108 (1986) 313–318.
[15] W.E. Whiteman, A.A. Ferri, Suppression of bending-torsion flutter through displacement-dependent dry friction damping, *AIAA Journal* 37 (1) (1999) 79–83.
[16] A.A. Ferri, Friction damping and isolation systems, *ASME Journal of Vibration and Acoustics* 117B (1995) 196–206.
[17] S. Natsiavas, Stability of piecewise linear oscillators with viscous and dry friction damping, *Journal of Sound and Vibration* 217 (3) (1998) 507–522.
[18] S. Natsiavas, G. Verros, Dynamics of oscillators with strongly nonlinear asymmetric damping, *Nonlinear Dynamics* 20 (1999) 221–246.
[19] S.W. Shaw, On the dynamic response of a system with dry friction, *Journal of Sound and Vibration* 108 (2) (1986) 305–325.
[20] J.A. Inaudi, G. Leitmann, J.M. Kelly, Single-degree-of-freedom nonlinear homogeneous systems, *ASCE Journal of Engineering Mechanics* 120 (7) (1994) 1543–1562.
[21] A.A. Ferri, B.S. Heck, Analytical investigation of damping enhancement using active and passive structural joints, *AIAA Journal of Guidance, Control, and Dynamics* 15 (5) (1992) 1258–1264.